

Structural Evolution of Sequentially Evaporated (Cs,FA)Pb(I,Br)₃ Perovskite Thin Films via In Situ X-Ray Diffraction

Karl L. Heinze, Tobias Schulz, Roland Scheer, and Paul Pistor*

Evaporation of perovskite thin films for solar cell applications is a solvent-free, well controllable, and scalable deposition path with promising prospects for commercialization. Compared to commonly applied simultaneous co-evaporation of various halide precursor salts, sequential evaporation followed by an annealing step allows to better control the amount of deposited precursors, and has the potential to largely improve reproducibility. In this work, Cs/formamidinium (FA)-based lead iodide perovskites are deposited via sequential evaporation in a vacuum chamber and the phase formation and evolution of different precursor-stacking sequences and annealing conditions are investigated with in situ X-ray diagnostics. In addition, some Br is added to investigate the effect of halide intermixing. The stacking sequence is found to strongly influence the formation of dominant phases as well as the preferential orientation and HGH morphology of the as-deposited films. These variations in turn affect the diffusion and conversion during thermal annealing and ultimately the conversion ratio of the final perovskite layers. For example, it is found that starting the stacking sequences with the A cations (CsI, FAI) favors a fast and complete conversion of the perovskite phase. However, the result is the formation of perovskite layers with large voids.

deposition technique is spin-coating, which bears two main disadvantages. Spin-coating cannot be upscaled to produce devices on large areas for industrial applications, and solvents such as dimethylformamide or dimethylsulfoxide are needed.^[3,4] These solvents are toxic^[5] and costly, have a bad environmental footprint,^[6] can cause damage to underlying layers^[7] and thus their usage is ideally minimized.

A completely solvent-free perovskite synthesis can be realized by evaporation via physical vapor deposition (PVD), which allows for homogeneous large area growth on various substrate morphologies.^[8–12] Compared to co-evaporation, sequential evaporation enables good crystallinity and better process control.^[8,13,14] Feng et al. have shown that homogenous formamidinium (FA)-based perovskite layers can be deposited with a sequential roll-to-roll process on large areas, and applying an optimized low temperature annealing at 60 °C a high PCE of 21.3% could be obtained.^[6] A record PCE of 24% for sequentially deposited

CsFAPbI₃ was reported by Li et al. in 2022.^[15] In sequential lead halide perovskite deposition, usually the inorganic components, typically PbI₂, are deposited first, and their properties and morphologies might therefore strongly influence subsequent perovskite formation. For sequential wet-chemical processing routes, i.e., the so-called two-step-deposition methods, many reports focus on the optimization of the inorganic precursor deposition in view of solar cell performance, emphasizing its significance. There, solvent additives or variations of different preparation techniques are used to obtain optimal morphologies,^[16–18] and the consensus is that a highly oriented and porous PbI₂ precursor layer favors a full conversion to the perovskite phase leading to high-performance PSCs.^[19–23]


However, few reports exist regarding the optimization of the inorganic precursor deposition in the context of PVD. Instead of a solution penetrating the inorganic precursor, during sequential evaporation a condensed organic (e.g., formamidinium iodide [FAI]) layer is formed, and solid-state diffusion determines the reaction kinetics. As a consequence, optimal precursor morphologies for a fast and complete conversion into high-quality perovskite layers might be different for vacuum-based approaches as compared to a solution-based conversion step. Using PVD, Hoerantner et al. speculate that the porosity of PbI₂ could be

1. Introduction

Perovskite solar cells (PSCs) have almost reached the power conversion efficiency (PCE) of silicon-based solar cells (26.1% and 26.8%, respectively^[1,2]). However, to date, the most prominent

K. L. Heinze, T. Schulz, R. Scheer
Thin Film Photovoltaics
Martin-Luther-University Halle-Wittenberg
Von-Danckelmann-Platz 3, 06120 Halle (Saale), Germany

P. Pistor
Center for Nanoscience and Sustainable Technologies (CNATS)
Universidad Pablo de Olavide
Carretera de Utrera 1, 41013 Sevilla, Spain
E-mail: ppis@upo.es

 The ORCID identification number(s) for the author(s) of this article can be found under <https://doi.org/10.1002/pssa.202300690>.

© 2023 The Authors. physica status solidi (a) applications and materials science published by Wiley-VCH GmbH. This is an open access article under the terms of the Creative Commons Attribution-NonCommercial License, which permits use, distribution and reproduction in any medium, provided the original work is properly cited and is not used for commercial purposes.

DOI: 10.1002/pssa.202300690

advantageous for its conversion to MAPbI_3 .^[24] Li et al. maximized their PCE by enhancing the crystallinity of their PbI_2 seed layer and produced a smoother and more condensed surface by incorporating a small amount of CsI and PbCl_2 .^[15] Wang et al. employ spin-coated $\text{PbI}_2/\text{PbCl}_2$ and find larger precursor grains to be beneficial for perovskite formation during FAI evaporation.^[14] The optimization of the PbI_2 precursor layer is even more important, as PbI_2 is a highly versatile material with many different polytypes^[25] and morphologies, and its full potential for optimized sequential evaporation is still to be unfolded.

Solid-state diffusion through PbI_2 is driven by concentration gradients. However, there is still limited knowledge and understanding about the interdiffusion during the annealing of the precursors for perovskite conversion. As the lead halide salts share a similar octagonal lead halide configuration in the lead halide precursor as in the final perovskite phase, the conversion is sometimes called intercalation of the A cation. For MAPbI_3 , Eames et al. found that primarily I^- and MA^+ diffused within the perovskite lattice, while the Pb^{2+} ions mostly remained stationary.^[26] This effect has been scarcely discussed for FA-based perovskites up to now and our experiments are specifically designed to elaborate on this knowledge gap.

Therefore, we investigate the sequential deposition of $(\text{Cs, FA})\text{Pb(I, Br)}_3$ thin films via sequential thermal evaporation of the precursors in a vacuum chamber followed by an annealing step. We prepare perovskite absorbers using different sequences of the components FAI, cesium iodide (CsI), lead iodide (PbI_2), and lead bromide (PbBr_2) and analyze the crystal structure evolution of the different phases present during deposition and post annealing. For this purpose, we use an in situ X-ray diffraction (XRD) setup,^[27] which allows us to observe the evolution of crystalline phases during growth and annealing. In the first part of this work, the iodine-based perovskite $(\text{Cs, FA})\text{PbI}_3$ is synthesized comparing two different precursor stacks: the conventional one starting with the B cation (Sequence B, $\text{PbI}_2\text{-FAI-CsI}$) and an alternative approach where the PbI_2 is deposited last (Sequence A, CsI-FAI-PbI_2). We detect large differences in the preferred phase formation, phase evolution during annealing, and morphology using in situ XRD, scanning electron microscopy (SEM), and energy-dispersive X-ray spectroscopy (EDX) measurements. The in situ XRD allows us to distinguish between the growth of two different PbI_2 polytypes: the hexagonal 2H phase and the rhombohedral 6R phase. Our results give evidence that the different precursor configurations can have a large impact on the conversion and final perovskite formation. In addition, we explore different options to optimize conversion into the perovskite phase such as nonstoichiometric precursor ratios, the deposition of split/multiple precursor layer stacks or the variation of the precursor morphologies by varying the substrate temperature during deposition. Finally, we investigate how the introduction of small amounts of Br in the form of PbBr_2 affects the aforementioned and analyze two different precursor sequences for the deposition of the mixed-halide perovskite $(\text{Cs, FA})\text{Pb(I, Br)}_3$: one similar to sequence B, where the lead halides are deposited first ($\text{PbBr}_2\text{-PbI}_2\text{-FAI-CsI}$) and one where they are evaporated first and last, respectively ($\text{PbBr}_2\text{-FAI-CsI-PbI}_2$). We observe a strong effect of the sequence on the formation of preliminary Br-rich and

I-rich phases and their reaction speed toward a single mixed-halide perovskite phase.

2. Results

In total, we have conducted three different experimental series. In the first set of experiments, we compare different stacking orders of the precursors for the sequential formation of $(\text{Cs, FA})\text{PbI}_3$, namely depositing the A cations first (sequence A: CsI-FAI-PbI_2) and B cation first (sequence B: $\text{PbI}_2\text{-FAI-CsI}$). This is followed by precursor sequences where the PbI_2 layer is split into two parts with different ratios (sequence with split PbI_2), one of them at the bottom of the precursor stack, and the other on top (see **Figure 1**). Based on these simple experiments, we conduct a second series of experiments in the attempt to improve the conversion of the precursors into a perovskite film by comparing different processing conditions where the PbI_2 layer is deposited first (in that sense, variation of sequence B): PbI_2 layers synthesized at different process conditions (substrate temperature, wet-chemical deposition) and by applying overstoichiometric (os) amounts of FAI. The single component thicknesses were 21, 224, and 261 nm for CsI , FAI, and PbI_2 in each respective sequence. Details can be found in the Experimental Section.

Finally, we briefly investigate how the addition of PbBr_2 as a source of Br to the precursor layer stack impacts the film formation and perovskite conversion in the last series of experiments. In these layer stacks, CsI and FAI thicknesses were again 21 and 224 nm, respectively, while 106 nm of PbI_2 and 115 nm of PbBr_2 were evaporated. We will start with the thorough analysis of the phase formation and evolution through deposition and annealing of the precursor stack with the A cation at the bottom (sequence A).

2.1. Precursor Order I: CsI/FAI First, PbI_2 Last (Sequence A)

Sequence A is a novelty for sequential evaporation of perovskites and thus promises to give valuable insight into the growth and reaction dynamics of the layer stack. The in situ diffractograms recorded during the deposition of sequence A are depicted as color plots in **Figure 2a**. Here, the XRD intensity is color coded and the x/y axes correspond to the process time and the 2θ angle, respectively. Above the color plot, the respective deposition rates of CsI (blue background), FAI (red), and PbI_2 (yellow) are shown. Below the color plot, the peak area (given as integrated intensity: Int. I) evolution of the most relevant peaks for each precursor component and phase is depicted. The representative peaks

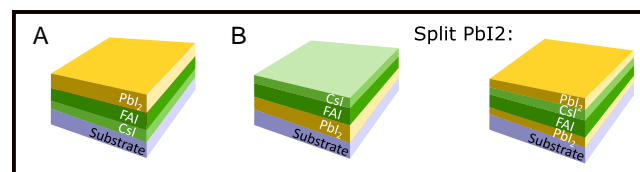


Figure 1. Schematic layer stacks after evaporating A, B, and split PbI_2 sequences. The layers providing A cations CsI and FAI are shown in light and dark green, respectively. PbI_2 layers are yellow.

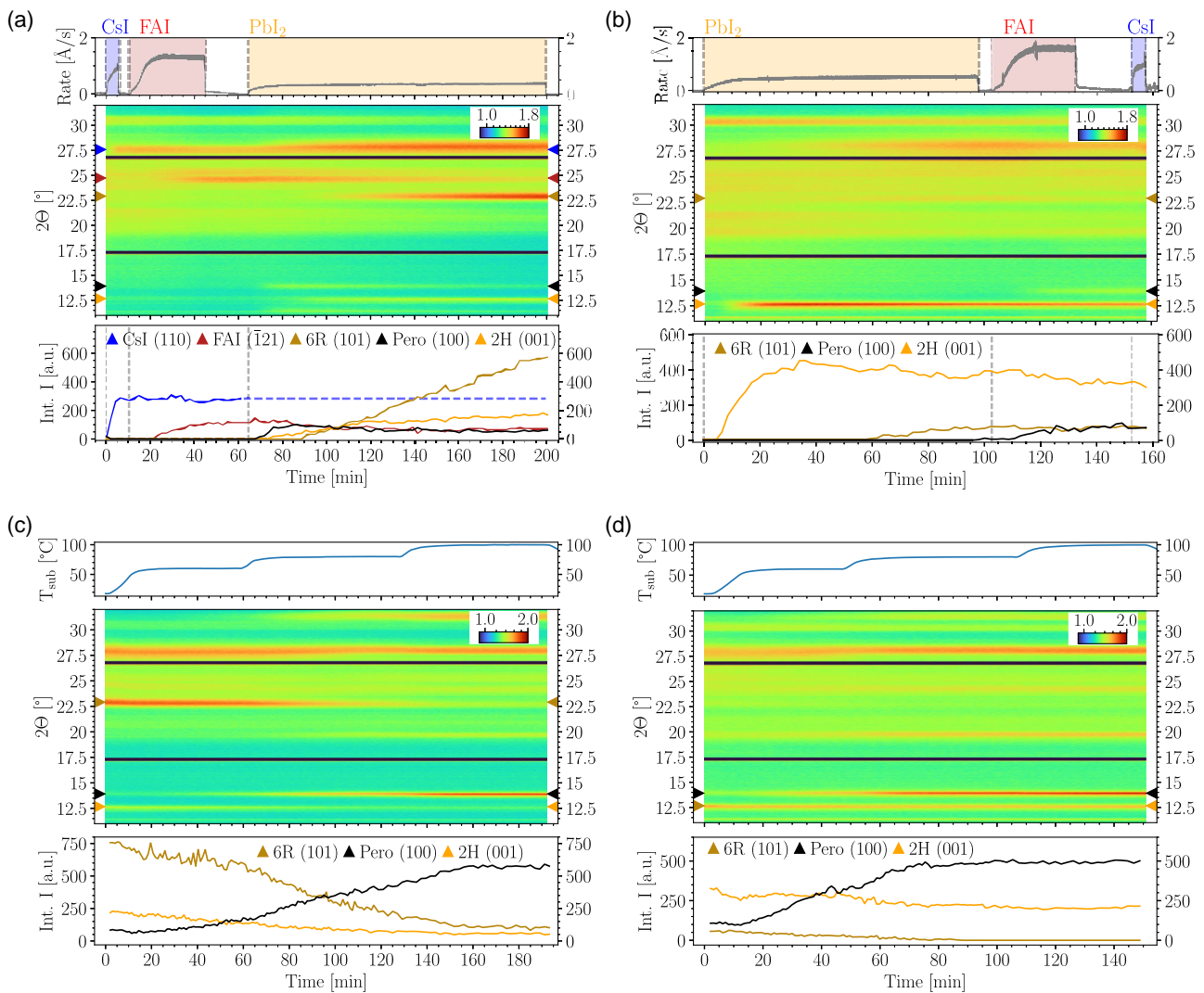


Figure 2. Process diagrams for evaporation of sequences a) A and b) B: The diagrams include rates of CsI–FAI–PbI₂ (blue, red, and yellow backgrounds, respectively–top), in situ XRD color plot (center) and development of integrated peak intensities (Int. I–bottom). Corresponding 2θ peak positions for evaluated peaks from the literature are displayed as triangles next to the color plot. In sequence A, CsI (110) Int. I is continued as a constant dashed line during PbI₂ deposition since evaluation is made impossible due to superposition with (Cs, FA)PbI₃ (200) (labeled Pero) and PbI₂ 6R (104) peaks, both broad near 28°. [25,29,31] In sequence B, FAI and CsI Int. I are not shown, since their intensities are too low. Process diagrams of sequences c) A and d) B during annealing: The diagrams show substrate temperature (top), in situ XRD color plot (center) and integrated intensity (Int. I) peak development (bottom). The sample temperature is increased from 60 to 100 °C over 150 min to fully convert the layer stack to the perovskite α phase.

shown here are marked by triangles next to the color plot, according to the literature value of their respective 2θ positions. Before evaporation, substrate peaks at 20°, 21.5°, 30.5°, and 35.4° are visible, mainly from the cubic indium tin oxide (ITO) phase. [28] These are attenuated during the evaporation process due to absorption of X-rays in the deposited layers. To evaluate the formed crystalline phases in more detail, θ–θ scans of the layers directly after deposition and after annealing (i.e. at the end of each color plot) are shown in Figure S4 (Supporting Information). During the first evaporation step, the characteristic (110) peak of the cubic CsI phase appears at 27.6°. [29] Throughout the later stages of this process, superposition of this peak with peaks from other phases impedes its quantification, and as a

simplification we assumed its intensity to be constant during PbI₂ deposition (indicated by the dashed line). After 22 min, the FAI monoclinic crystal phase becomes visible with its main peak at 24.7° corresponding to the (121) lattice plane. [30] Subsequently, during PbI₂ evaporation, first the characteristic (100) peak of the FAPbI₃ perovskite α phase at 13.9° appears [31] after approximately 70 min of processing time. At this point, we cannot determine, if the perovskite α phase contains low amounts of Cs, so we will refer to the α phase as (Cs, FA)PbI₃ (labeled Pero in Figure 2). Please note that, while we do observe a low intensity peak at 11.5°, close to the (001) peak of the FAPbI₃ δ phase, [32] we assume that no δ phase is formed, as explained in the SI on the basis of Figure S1 (Supporting

Information). FAI and (Cs, FA)PbI₃ peaks decrease in intensity slightly starting at 80 min and shortly after the (001) peak of the hexagonal PbI₂ 2H phase at 12.7° forms.^[33]

Starting at 90 min, a peak at 22.9° dominates during PbI₂ evaporation and the 2H (001) peak shrinks. The newly observed peak at 22.9° is strongly shifted compared to the 2H (100) peak at 22.5°.^[33] We deduce that the PbI₂ phase not only undergoes a change in preferential orientation, but a different phase starts to grow. We allocate this to the PbI₂ 6R phase (see Figure S2, Supporting Information), which exhibits one of its main peaks at 22.9°, stemming from its (101) lattice plane. The 6R phase has been observed to develop via evaporation under vacuum conditions.^[25] In our experiment, the 6R (101) peak then grows linearly, making up all the crystalline PbI₂ phase growth visible in the diffractograms. The 6R (104) peak at 28.3° also develops clearly, but cannot be quantified due to superposition with the CsI (110) and (Cs, FA)PbI₃ (200) peaks. The transition from the growth of the 2H to the growth of the 6R polytype is a trend observed in many of our PbI₂ layers grown under vacuum (Figure S3, Supporting Information). For a summary of the most relevant peaks, see **Table 1**.

To investigate the conversion into the perovskite thin film resulting from sequence A, the layer was annealed at three different temperatures (Figure 2c). The top graph shows the substrate temperature, while the peak area development is displayed at the bottom. At 60 °C, a slow reaction between the three precursor layers takes place, resulting in a slow increase of the (Cs, FA)PbI₃ (100) peak intensity. Increasing the substrate temperature to 80 °C enhances this reaction, as (Cs, FA)PbI₃ (110) and (210) peaks appear at 19.7° and 31.4°, respectively. At the same time, the triple peak at 28° begins to narrow down to a single peak. This hints toward an amorphization of CsI or, more likely, diffusion of CsI into the perovskite layer. We suspect the (Cs, FA)PbI₃ (200) peak to be dominant at 28° due to PbI₂ conversion to the perovskite phase. Simultaneously, the 2H (001) and 6R (101) PbI₂ peaks begin to decrease in intensity. After approximately 150 min and at a temperature of 100 °C, the reactions described earlier are concluded and peak developments come to a halt in the timescale visible in our experiment. Perovskite peaks dominate the resulting layer and only slight traces of residual PbI₂ and FAI remain visible.

2.2. Precursor Order II: PbI₂ First (Sequence B)

Sequence B is the usual deposition order for sequentially evaporated perovskites and the logical counterpart to sequence A. We investigate this sequence via in situ XRD to expand the understanding on the reaction kinetics between precursor layers during evaporation and annealing. For sequence B PbI₂, FAI, and CsI were evaporated sequentially in this order. The in situ process diagram is shown in Figure 2b. Upon PbI₂ evaporation, a strong 2H (001) peak develops, which saturates after 30–40 min and then decreases in intensity slightly, while the 6R (101) and (104) peaks, respectively, evolve. FAI evaporation starting at 102 min leads to the formation of FAPbI₃ as can be seen by the low intensity (Cs, FA)PbI₃ (100) peak. Neither FAI nor CsI peaks appear in the XRD during their respective evaporation step, suggesting either strong diffusion and reactivity and/or low crystallinity of the unreacted species.

During annealing of sequence B (Figure 2d), the layer stack reacts well and all major perovskite peaks develop, increasing in intensity with each temperature step (60 °C, 80 °C, and 100 °C). Still, a small residual 2H (001) peak remains. FAI re-evaporation is an unlikely cause for remaining PbI₂, since we were only able to evaporate FAI above 140 °C in vacuum. At standard conditions, FAI has been shown to evaporate at 230 °C.^[30] In consequence, the incomplete reaction of the layer stack is not a result of FAI desorption, but indicates that the provided heat does not enhance diffusion enough to fully react the layer stack during our experiment. This is consistent with the correct stoichiometry of annealed films (as correct by EDX, see the next paragraphs).

2.3. SEM and EDX

The characteristics of sequences A and B are further investigated by SEM and EDX measurements. The SEM cross section of sequence A in **Figure 3a** shows a homogeneous bulk with distinct properties at the surface and the substrate interface. At the surface small, bright crystallites and platelets can be seen. These are assigned to PbI₂ surface species. At the NiO interface, clearly visible voids suggest a peculiar upward diffusion behavior of the A cations into the PbI₂. We use EDX to

Table 1. Overview of relevant reference 2θ diffraction peaks for the evaporated components. 2H and 6R refer to different polytypes of the PbI₂ compound with hexagonal and rhombohedral crystal structures, respectively. I-rich (IPer) and Br-rich (BrPer) perovskite phases do not correspond exactly to the FAPbI₃ and FAPbBr₃ phases and XRD peaks given here, since IPer and BrPer phases might include varying shares of the respective other halide, resulting in a shift of the peak positions. Additionally, the incorporation of CsI leads to a small shift to higher diffraction angles.

Material	Crystal Structure	Space Group	Lattice Plane	XRD 2θ Angle	Source
CsI	Cubic	Pm-3m (221)	(110)	27.6°	[29]
FAI	Monoclinic	P21/a (14)	($\bar{1}$ 21) (002)	24.7°, 25.6°	[30]
PbI ₂	2H	P-3m1 (164)	(001) (002)	12.7°, 25.5°	[33]
PbI ₂	6R	R-3m (166)	(101) (104)	22.9°, 28.3°	[25]
FAPbI ₃	Cubic	Pm-3m (221)	(100) (110) (111) (200) (210)	13.9°, 19.7°, 24.2°, 28.0°, 31.4°	[31]
PbBr ₂	Orthorhombic	Pnam (62)	(200) (111) (220)	22.0°, 22.7°, 29°	[40]
FAPbBr ₃	Cubic	Pm-3m (221)	(100) (110) (200)	14.8°, 20.9°, 29.8°	[67]

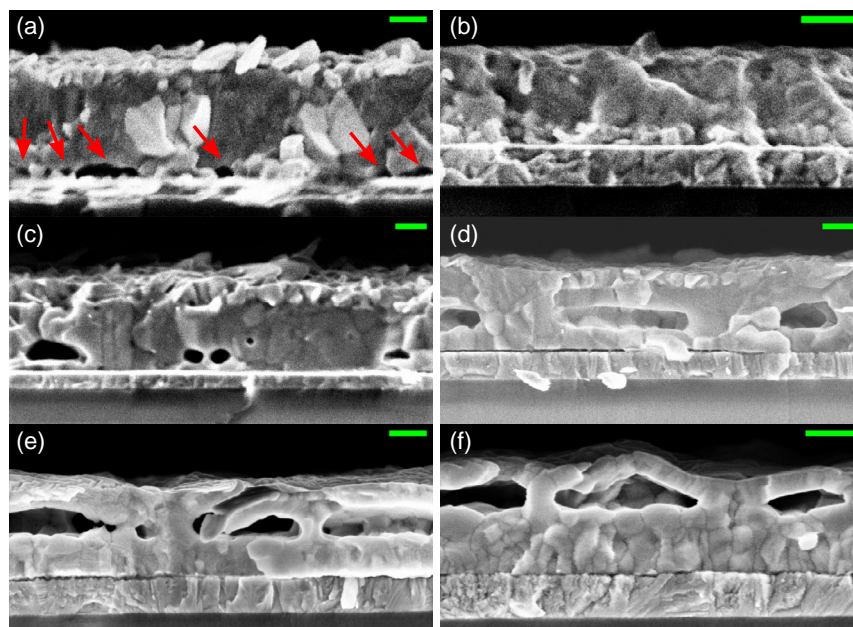


Figure 3. Scanning electron microscopy (SEM) cross sections after annealing. a) Sequence A (CsI-FAI-PbI₂). Voids at the interface to the substrate are marked by red arrows. b) Sequence B (PbI₂-FAI-CsI) after annealing. c–f) Processes with split PbI₂ (sequence [x]PbI₂-FAI-CsI-(1-x)PbI₂) after annealing with $x = 10\%$, 30% , 50% , 70% . The green scale bar represents 200 nm.

Table 2. Ratios of X/Pb determined via EDX for different evaporation sequences for the perovskite films after annealing. X corresponds to I for sequences resulting in (Cs, FA)PbI₃ and represents the sum of I and Br for mixed-halide processes Br-1 and Br-split. Please note that the quantification of the Br halide with EDX exhibits a relatively large experimental error. For a stoichiometric perovskite, an X/Pb ratio of 3 is expected.

Sequence	Materials	X/Pb ratios
A	CsI-FAI-PbI ₂	3.04
B	PbI ₂ -FAI-CsI	3.08
Br-1	PbBr ₂ -PbI ₂ -FAI-CsI	3.47
Br-split	PbBr ₂ -FAI-CsI-PbI ₂	3.27

quantify the stoichiometry in our samples. Since the organic components in FAI cannot be quantified well with our EDX system, we use the I/Pb ratio as a manner to quantify the composition. Measurements for sequences A and B are shown in Table 2. The sample from sequence A exhibits a near-perovskite stoichiometry, in good agreement with the XRD results.

The SEM image of sequence B in Figure 3b depicts a bulk with visibly larger crystallites compared to A, while exhibiting a thin, separated layer close to the substrate. As this layer appears brighter in the SEM image, we assume that it is PbI₂ rich. Therefore, the unreacted crystalline PbI₂, observed by XRD, is located at the NiO interface, as one could expect from the evaporation sequence. Similar to sequence A, the EDX measurements in Table 2 show a near-perovskite stoichiometry. Considering the PbI₂ at the bottom and the I/Pb ratio of 3, this suggests some remaining unreacted FAI and CsI resulting from lack of

diffusion. Noticeably, no voids are visible at the NiO interface, supporting the idea of an A cation-dominated diffusion.

2.4. Precursor Order III: PbI₂ at the Top and at the Bottom (Sequence with Split PbI₂)

To investigate the A cation diffusion behavior more deeply and in an attempt to achieve a more homogeneous film formation, we tested splitting the evaporated PbI₂ layer and depositing different shares x (and $1-x$) of PbI₂ first (and last): (x)PbI₂-FAI-CsI-(1-x)PbI₂. We achieved a full reaction to the perovskite α phase with $x = 10\%$, 30% , 50% , and 70% according to XRD (Figure S5–S7, Supporting Information). However, we were not able to suppress the void formation, as long as part of the PbI₂ was evaporated last. Instead, the position of the voids moved upward in the perovskite layer with increasing x . As can be seen in the respective SEM images (Figure 3c–f), the voids mark the position of the FAI layer prior to annealing.

2.5. Modifications of Sequence B (PbI₂ First)

So far it was found that sequences A and precursor order III caused void formation and can therefore lead to mechanical destabilization of the layer. Consequently, we explored several modified paths for sequence B to achieve full conversion to the perovskite phase. To drive the conversion of the residual, unreacted PbI₂ in sequence B, we I) supplied an os amount of FAI, II) used cooled (-30°C) and heated ($100, 170^\circ\text{C}$) substrates only during PbI₂ deposition to benignly alter the PbI₂ properties and (III) employed the spin-coating technique to fabricate a completely different PbI₂. A schematic overview of the modifications is provided in Figure 4.

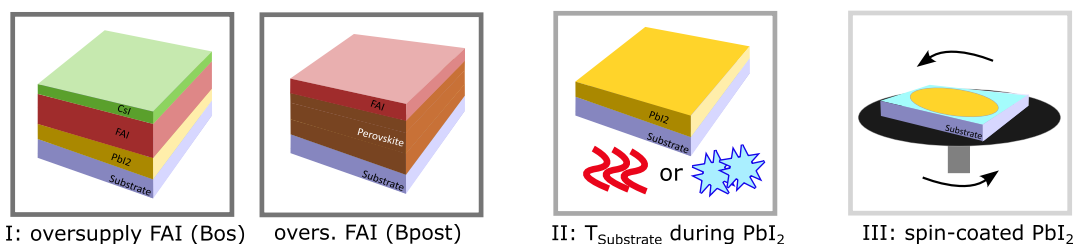


Figure 4. Schematic overview of modifications of sequence B (PbI_2 first). From left to right: I: oversupply of FAI during deposition (Bos) or as a post treatment (Bpost); II: substrate temperature during PbI_2 deposition; and III: spin-coated PbI_2 .

2.5.1. I: Oversupply of FAI

To provide an oversupply of FAI, we deposited the full PbI_2 layer first, but drove further reaction either by directly evaporating an os amount of FAI in the sequence Bos: PbI_2 –(os)FAI–CsI or by post depositing additional FAI in the sequence Bpost: PbI_2 –FAI–CsI–(post)FAI. Both modifications successfully lead to a full conversion of the layer to the α perovskite phase, as can be seen in Figure S8 (Supporting Information). In the cross-sectional SEM images of Bos and Bpost (Figure S9, Supporting Information), the layer stack is fully reacted. We observe a dependence of the crystallite size on the position in the layer, with larger grains toward the top. This is assumed to be related to a stoichiometry gradient in the layer. As has been shown previously, a larger concentration of A cations can lead to an increase in crystallite size.^[34–36] Additionally, the pinholes in the top layer caused by the electron beam point to an organic-rich stoichiometry. Therefore, we assume that the reaction in our layers is still diffusion-limited and the FAI is not distributed completely homogeneously.

2.5.2. II: Substrate Temperature during PbI_2 Deposition

In our evaporation process, PbI_2 tends to grow with weak preferential orientation and in a porous manner (SEM cross section in Figure S10, Supporting Information). Similar behavior was observed by other groups by growth of porous, polycrystalline PbI_2 films with small crystallite sizes.^[24,37,38] Other publications have shown that PbI_2 can be evaporated as a compact layer with strong preferential orientation^[6] and low roughness.^[15] In an attempt to ameliorate the PbI_2 properties for the diffusion reaction process, we deposited PbI_2 at different substrate temperatures (–30, 100, and 170 °C; SEM in Figure S11, Supporting Information). Both heating and cooling resulted in strongly 2H-dominated growth modes of PbI_2 . However, none of the layer stacks were fully converted to the perovskite phase, even though the PbI_2 morphology and texture was strongly altered (Figure S12 and S13, Supporting Information). So far, only sequence A and the processes with split PbI_2 resulted in fully converted layers without excess A cations. All of these exhibit 6R growth giving rise to the idea that the diffusion–reaction kinetics of the perovskite conversion benefit from the presence of this PbI_2 species.

2.5.3. III: Spin-Coated PbI_2

In an additional experiment, we first spin-coated a layer of PbI_2 and achieved a more homogeneous, smooth PbI_2 growth (SEM

cross section in Figure S14, Supporting Information). For this sample, high-intensity perovskite peaks appear already during evaporation of FAI and CsI. Here, the perovskite peaks during evaporation are much larger than for evaporated PbI_2 in sequence B. Subsequently, we observe a clear (Cs,FA) PbI_3 (100) peak shift during evaporation of CsI (Figure S15, Supporting Information). In the SEM cross section of the finished layer, large columnar perovskite crystallites can be seen (Figure S16, Supporting Information). In contrast to the previous attempts with evaporated PbI_2 , here the perovskite crystallites stretch through the full layer. The qualities of an evaporated PbI_2 precursor could potentially be improved by co-evaporating CsBr or PbCl_2 and CsI, as has been successful in other works.^[15,39] Further ideas will be touched upon in the discussion section. We conclude that the PbI_2 morphology strongly impacts the reaction and diffusion dynamics of the perovskite conversion. The results with spin-coated PbI_2 show that the A cations' diffusion–leading to perovskite conversion–can be optimized and a compact PbI_2 host structure can be beneficial for the transport and diffusion of the FAI.

2.6. Mixed I/Br Perovskites

Halide diffusion is a relevant aspect when preparing homogeneously mixed perovskite (Cs,FA) $\text{Pb}(\text{I},\text{Br})_3$ and ensuring the stability of a single stable phase. We prepared mixed I/Br perovskite compositions in two different sets of evaporation sequences (see Table 2).

2.6.1. Precursor Order I: Lead Halides PbX_2 First (Br-1)

For the sequence Br-1, we evaporated the sequence PbBr_2 – PbI_2 –FAI–CsI. During evaporation, the components crystallize with a strong preferential orientation, as can be seen in the process diagram in Figure 5a (Additional Θ – Θ scans in Figure S17, Supporting Information). First, orthorhombic PbBr_2 (200), (111), and (220) peaks appear at 22.0°, 22.7°, and 29°, respectively.^[40] Upon PbI_2 evaporation, some PbI_2 is incorporated into the PbBr_2 structure as we observe in a peak shift of PbBr_2 (111) peak by 0.07° (Figure S18, Supporting Information). The PbBr_2 incentivizes the PbI_2 to grow only in the 2H phase, as only the correspondent (001) and (002) peaks appear.^[33] Peaks corresponding to the 6R polytype do not evolve. We were able to confirm these observations concerning preferential orientation and polytype during evaporation of an additional process, where only PbBr_2 – PbI_2 were deposited (Figure S19, Supporting

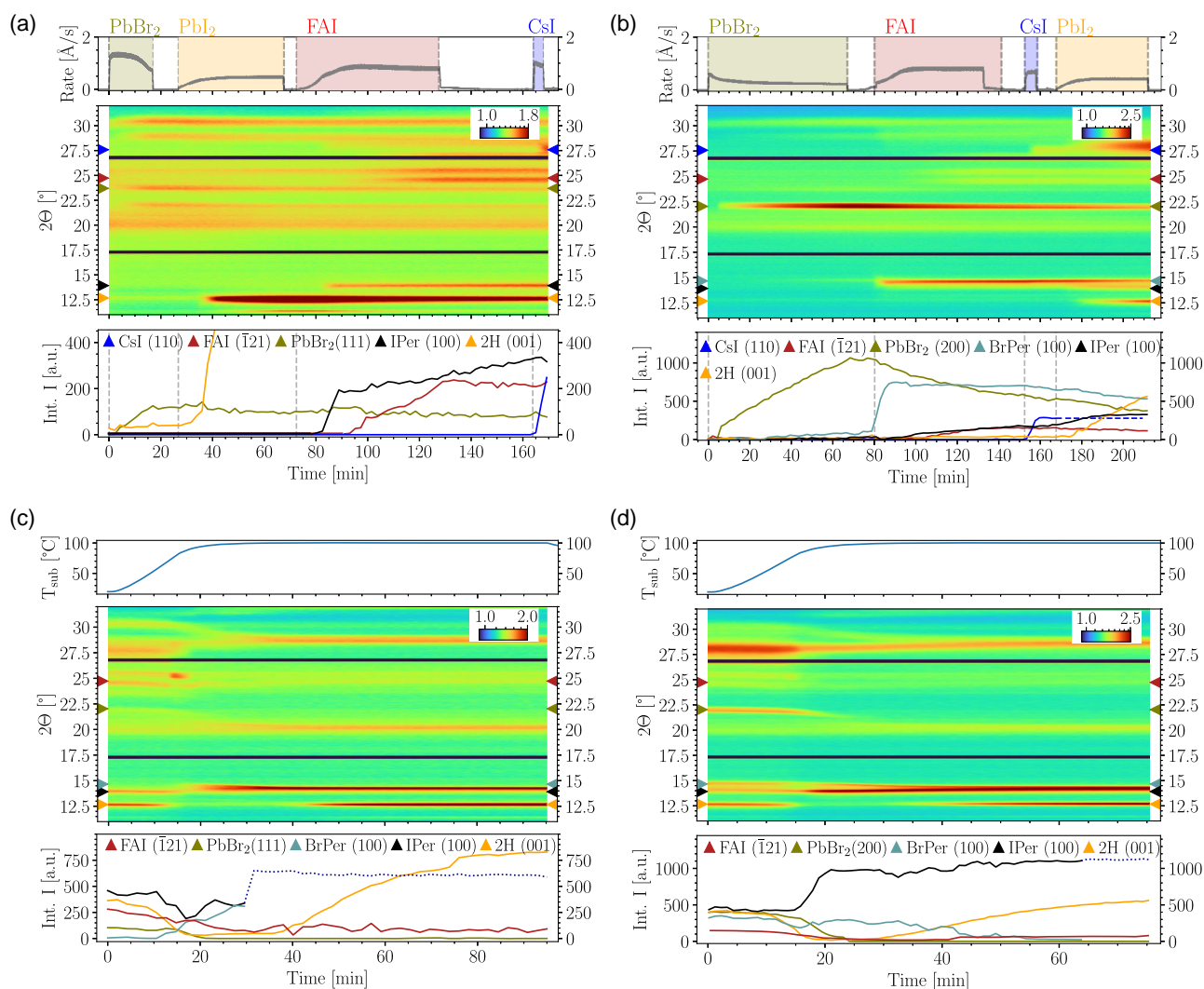


Figure 5. Upper: process diagrams for evaporation of sequences a) Br-1 and b) Br-split including rates during single component deposition (top), in situ XRD color plot (center) and representative peak evaluation (bottom) given as the integrated intensity (Int. I) of each peak over time. Triangles next to the color plot give literature 2θ positions for the evaluated experimental peaks. In sequence Br-split, CsI (110) Int. I is continued as a dashed line due to superposition with IPer (200) and 6R (104) peaks, both broad near 28° .^[25,29,31] Lower: process diagrams for annealing of c) Br-1 and d) Br-split consisting of substrate temperature (top), in situ XRD color plot (center) and Int. I of significant peaks.

Information). In Br-1, the 2H (001) Int. I increases quickly during PbI_2 evaporation and decreases upon the subsequent evaporation of the A cations (detailed development shown in Figure S18, Supporting Information). During the FAI-deposition step, I-rich (Cs, FA)Pb(I, Br)₃ perovskite (IPer) (100) and (200) peaks are formed first.^[31] Subsequently, the monoclinic FAI phase is formed, manifested through the appearance of a double peak at 24.7° and 25.6° .^[30] Upon CsI evaporation, we observe no shift in the IPer (100) peak (Figure S20, Supporting Information) and CsI crystallizes, noticeable for example by the cubic phase (110) peak.

During annealing of Br-1 (Figure 5c), the 2H (001) peak is the first to rapidly lose intensity, indicating the commencement of the perovskite formation. After 13 min, FAI ($\bar{1}21$) disappears and 2 min later the perovskite (111) peak at 24.2° takes its place.^[31] Also after 13 min, FAI (002) shows an intensity jump,

hinting toward a recrystallization of the FAI in its orthorhombic phase.^[30] CsI starts reacting after 17 min at 88°C , as can be seen from the disappearance of its (110) peak.

All initial peaks exhibit a shift to lower angles due to thermal expansion. However, the PbBr_2 (111) peak shifts stronger than expected only from thermal expansion, indicating an incorporation of PbI_2 into the lattice (Figure S21 and S22, Supporting Information).^[41] After 15 min and at 80°C , the Br-rich (Cs, FA)Pb(I, Br)₃ perovskite phase (BrPer) (100) peak at 14.6° increases at the expense of the IPer (100) peak. Both peaks begin shifting toward each other (Figure S23, Supporting Information) and cannot be distinguished from 30 min onward (dotted line in Figure 5c). Further, BrPer and IPer peaks combine at around 20° and 29° , respectively, indicating that a single mixed perovskite (Cs, FA)Pb(I, Br)₃ phase has formed. Up until the end of the annealing, the double halide perovskite (100) intensity declines

slowly, while the 2H (100) intensity increases monotonously, indicating a slow recrystallization and/or decomposition process.

2.6.2. Precursor Order II: Lead Halides PbX_2 First and Last (Br-Split)

We then evaporated the sequence Br-split: PbBr_2 –FAI– CsI – PbI_2 (process diagram in Figure 5b and Θ – Θ scans in Figure S17, Supporting Information). After deposition of PbBr_2 and throughout FAI evaporation, both components quickly react to form both BrPer (100) and IPer (100) peaks. Later during FAI evaporation, an unreacted FAI phase forms. In contrast to Br-1, part of the deposited CsI is immediately incorporated into the BrPer phase, as indicated by a BrPer (100) peak shift toward higher angles (Figure S24, Supporting Information). Upon PbI_2 deposition, BrPer and IPer peaks clearly shift away from each other (Figure S24, Supporting Information), while the IPer (100) Int. I benefits from the I-rich evaporation step. After approximately 170 min, the 2H (001) peak evolves and grows quickly. Whether 2H or 6R PbI_2 growth dominates cannot be determined due to superposition of the 6R (104) peak with the perovskite peaks at 28° – 29° . While no 6R (101) peak is observed, a strong 2H (001) texture is induced in this sequence, as can be seen by its linear growth in Int. I.

During annealing of Br-split (Figure 5d), a conversion of the precursors to a highly oriented mixed-halide $(\text{Cs}, \text{FA})\text{Pb}(\text{I}, \text{Br})_3$ phase can be observed. After 10 min and at 50°C , the Int. I of the 2H (001) and PbBr_2 (200) peaks begin to decrease. Similar to Br-1, the peaks from both lead halide phases shift due to thermal expansion of the respective lattices and halide mixing (Figure S22, Supporting Information). After 25 min and at 98°C , they disappear completely. The PbI_2 2H (001) peak returns 5 min later and increases in size until the end of the annealing.

BrPer (100) and IPer (100) peaks shift toward each other starting at 17 min and 70°C (Figure S25, Supporting Information). The IPer (100) peak is strongly intensified. Both phases cannot be distinguished anymore after 65 min. It should be noted that the combined phase is formed much slower than in the Br-1 evaporation sequence.

The SEM images of Br-split and Br-1 are shown in Figure 6. As observed for the sequences with split PbI_2 , the deposition of FAI in between the lead halide layers in the sequence Br-split leads to void formation in the final film. In the top-view, unreacted PbI_2 forming island-type structures can be observed. Br-1 shows large crystallites throughout the whole interface and especially at the top. Still, the cross section displays PbI_2 residues at the substrate interface, which was to be expected from the in situ XRD results displayed in Figure 5c.

3. Discussion

We investigated the crystal growth and phase formation during variations of sequential evaporation and annealing processes for the preparation of $(\text{Cs}, \text{FA})\text{PbI}_3$ and $(\text{Cs}, \text{FA})\text{Pb}(\text{I}, \text{Br})_3$ using in situ XRD.

The approach to deposit A cations first via sequence A, as demonstrated for $(\text{Cs}, \text{FA})\text{PbI}_3$ in this work, is a novelty in the field of sequential perovskite evaporation. We observed that on top of the CsI/FAI stack, the PbI_2 precursor layer grew in the PbI_2 6R polytype, which, to the best of our knowledge, has not been reported for evaporated perovskite layers so far. Sequence A enabled complete transformation of the stoichiometric precursor layers into the perovskite, but also favored the formation of voids. These are potentially disadvantageous, as they could mechanically destabilize the perovskite layer. We reproduced this behavior in the sequence with split PbI_2 , where the voids shifted upward according to the thickness of the first PbI_2 layer and the position of the FAI layer.

In sequence B, we deposited a PbI_2 precursor layer first, which preferentially grew in the 2H polytype, transitioning to 6R later during deposition. We observed a good reactive behavior of the stoichiometric layer stack without void formation, but residual PbI_2 remained at the substrate interface even after prolonged annealing. This could not be avoided even in variations of this precursor sequence, where we deliberately changed the substrate temperature during PbI_2 deposition to see if we could stimulate the growth of PbI_2 with morphologies better suited for the conversion into perovskites. Finally, we were able to achieve full conversion into the perovskite phase for nonstoichiometric samples

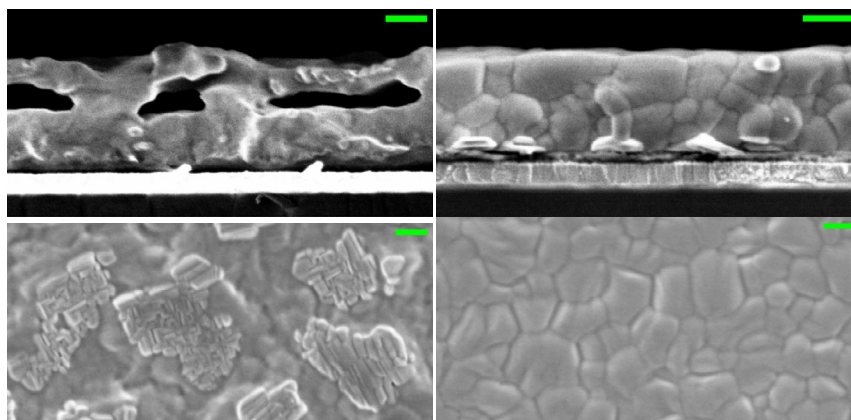


Figure 6. SEM cross sections (top) and top views (bottom) of Br-split (left) and Br-1 (right) after annealing. The green scale bars correspond to 200 nm. Similarly to the processes with split PbI_2 , Br-split displays voids from FAI diffusion and PbI_2 as well as PbBr_2 fixture. Br-1 exhibits large crystallites and unreacted PbI_2 at the substrate interface.

with the precursor sequence B by evaporating an excess of FAI during the same sequence (Bos) or as a post treatment (Bpost). While this is an interesting way to achieve the full conversion into the perovskite phase (no residual PbI_2), the impact of stoichiometry and precursor morphologies on the opto-electronic properties are still an open question and require further analysis.

3.1. FAI-Dominated Diffusion Leads to Voids

Our results strongly indicate that the reaction between FAI and PbI_2 is dominated by FAI diffusion into the PbI_2 layer. In sequences A and the sequence with split PbI_2 , this is clearly visible in the respective SEM images, where the FAI diffusion resulted in voids. Similar to MAI, FAI exhibits Volmer–Weber island growth (Figure S26, Supporting Information and refs. [42–44]). Therefore, the observed voids in sequence A could be explained by PbI_2 pillars growing next to FAI islands, thereby reaching the substrate interface and supporting the upward diffusion behavior of FAI. FAI from the substrate interface could diffuse into the PbI_2 host structure along these pillars, resulting in voids at the substrate interface.

A similar stack to our sequence with split PbI_2 was prepared by Yang et al. They evaporated an alternating sequence PbCl_2 –MAI– PbCl_2 –MAI, but did not observe voids in their layer after annealing.^[45] Comparing our sequence with split PbI_2 to Yang's work, it seems the A cation growth behavior is not decisive for the success of the diffusion reaction and perovskite transformation, since both MAI and FAI intrinsically exhibit island growth. However, the difference could originate from the properties of the lead halide layer. PbCl_2 can grow smoother than PbI_2 ^[44] or reduce roughness in PbI_2 as an additive,^[15] possibly enabling a homogeneous reaction along the surface in Yang's work. The PbI_2 evaporated in this work exhibits a rough surface and could amplify the island growth of FAI, resulting in void formation in the final film prepared via the sequence with split PbI_2 .

Sequence B is a well-known approach for sequential perovskite deposition. We observed that sequence B provided a less favorable perovskite conversion, making an excess of FAI necessary in the sequences Bos and Bpost to achieve a full conversion of the PbI_2 layer. For MAPbI_3 , some groups used an excess of A cations to transform the lead halide precursor layer and removed the excess A cation by annealing or washing.^[42,46] Sequence B has been used for perovskite device preparation and the effect of excess FAI on the optoelectronic properties has been shown to be advantageous for diodes and solar cells up to a certain excess value.^[34,35,47] However, other works have been successful in depositing a stoichiometric layer stack and fully converting it to the perovskite phase. Feng et al. deposited highly textured 2H PbI_2 and addressed underconversion by optimizing the post annealing temperature to drive FAI diffusion.^[6] In a noteworthy work, Moser et al. evaporated a PbI_2/CsBr precursor layer and achieved full conversion depositing FAI via chemical vapor deposition (CVD).^[39] Very recently, CsBr has been proposed to enhance diffusion and facilitate the full perovskite transformation in sequentially evaporated films.^[48] Full reaction was achieved more slowly in thicker layers of up to 400 nm as compared to multiply deposited layer stacks, and it was argued that this is due to diffusion limiting the reaction.^[48]

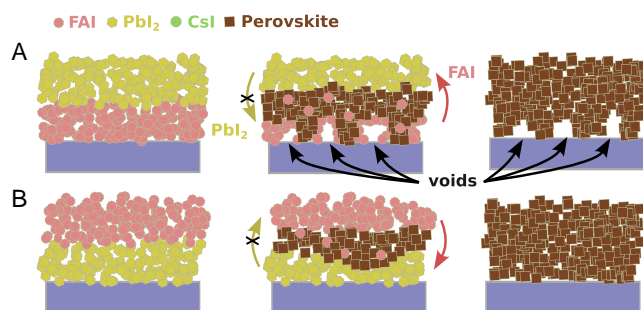


Figure 7. Simplified illustration of the proposed diffusion mechanism in a FAI– PbI_2 layer stack as in sequence A (top row) and a PbI_2 –FAI stack as in sequence B (bottom row). CsI is left out for simplicity. The left column presents the initial growth of layers during deposition, the center column illustrates the first reaction between the two layers and the right column shows a fully transformed perovskite layer after, e.g., annealing.

From our work and the aforementioned literature results, we suggest a simple mechanism (Figure 7): Upon contacting, FAI and PbI_2 layers react to form the perovskite FAPbI_3 , through which further FAI components will diffuse due to a concentration gradient and react with the PbI_2 on the other side and so on. This is made possible by the capacity of FAPbI_3 to hold and transport excess FAI.^[34–36] The PbI_2 provides the host structure for the interdiffusion of FAI and the properties of the PbI_2 host structure are therefore expected to directly influence the diffusion behavior of the FAI. It is unlikely that the FAI diffuses through the PbI_2 without reacting, since the enthalpy of formation of FAPbI_3 should be lower than that of its educts.^[49,50] CsI diffusion only takes place through already-formed FAPbI_3 , since CsI and PbI_2 do not interdiffuse or react to CsPbI_3 , unless 200 °C are applied, as confirmed by annealing of a layer stack in our in situ chamber by us (Figure S27, Supporting Information) and reported elsewhere.^[51] This type of diffusion reaction has been termed intercalation for MAI into PbI_2 ,^[52,53] but has not been described as clearly for the FAI into PbI_2 diffusion/reaction process.^[6,15,54]

In consequence of the suggested mechanism, in both sequences A and B, the diffusion and conversion into perovskite of the precursor stack depends strongly on the properties and morphology of the PbI_2 precursor, including important factors such as porosity, surface texture, preferential orientation, and polytype (2H or 6R). In the following, we will discuss the impact of these different PbI_2 properties on the reaction behavior of the layer stack.

3.2. PbI_2 Polytypes Influence Perovskite Formation

In our work, the different observed PbI_2 polytypes are expected to impact the diffusion/reaction processes involved in the perovskite conversion. In sequence A, when the PbI_2 was grown on top of the FAI precursor, the A cation precursor strongly promoted the growth of PbI_2 in the 6R polytype. In the sequences with split PbI_2 , the 6R growth was also enhanced in comparison to sequence B during evaporation of the second PbI_2 layer, when this contributed 70% and 90% of the total PbI_2 . In sequence B, PbI_2 is growing on top of the hole-transport layer (HTL) (NiO),

favoring 2H PbI_2 . During conversion, the 6R part of the PbI_2 layer was first converted, while parts of the 2H did not fully react. Obviously, this could be incentivized by the fact that the 6R-rich domain is located on top of the 2H domain (growth only at later process time) and thereby close to the A cation supply. Still, our results indicate that the 6R polytype could be preferable for the perovskite conversion.

The dependence of PbI_2 conversion on the favored polytype is scarcely discussed in perovskite literature, since other polytypes than 2H are rarely observed. Dhamaniya et al. use a solution additive to fabricate a PbI_2 precursor layer with similar structure as the 6R polytype observed in our work.^[55] They observe faster perovskite conversion during wet-chemical treatment and attribute this to higher porosity, surface roughness, and surface area of the new structure. Malevu et al. compare the influence of PbI_2 6R and 12R precursors on final perovskite device efficiency, but don't include the most common 2H polytype and their structural observations are limited.^[56] To the best of our knowledge, no other reports exist investigating other PbI_2 polytypes than 2H for sequential deposition, not to mention evaporation.

In our experiments, the preferential orientation of the 6R polytype did not seem to play a role, since (101) favored growth dominated in sequence A, while (104) dominated in the sequence with split PbI_2 and both enabled fully converted layer stacks. In sequence B, weakly oriented 2H PbI_2 remained partially unconverted, while strongly oriented spin-coated 2H PbI_2 enabled good conversion. Still, evaporated, strongly oriented 2H PbI_2 did not enable full conversion as we showed by deposition of PbI_2 at different substrate temperatures. Other works have concluded orientational properties of the precursor layer to be a decisive factor for conversion. For $(\text{Cs}, \text{FA})\text{PbI}_3$, a highly textured PbI_2 precursor layer was fabricated by Li et al, which included PbCl_2 and CsI to enable an isotropic growth of the precursor and full perovskite conversion.^[15] Another group used a vapor treatment to promote face-up orientation of the PbI_4^{4-} octahedra to enhance diffusion of MAI and conversion of PbI_2 to MAPbI_3 .^[38] Possibly, the influence of orientation on perovskite conversion is stronger for the 2H than for the 6R polytype.

We observed full conversion to the perovskite phase for both 2H and 6R polytypes in different preferential orientations. Thus, we suspect PbI_2 porosity to also play a role in the diffusion reaction. In sequence B, porosity could inhibit FAI diffusion into the PbI_2 by forming diffusion bottle necks or promoting Volmer–Weber island growth of the FAI. In sequence A, the pre-deposited FAI layer could suppress island growth of the PbI_2 and enable more homogeneous Stranski–Krastanov layer-plus-island or even Frank–van der Merwe layer-by-layer PbI_2 growth, resulting in a more compact structure for further reaction.

Several works have shown porosity of the PbI_2 precursor plays a role in two-step spin-coating, where a porous layer is mainly seen as an advantage for easier infiltration by the organic cation solution.^[21,57–59] Astonishingly in blade-coating, compactness has been observed to be more favorable for conversion.^[60] However, porosity versus compactness is a blank slate in the field of sequential evaporation and uniform quantification is needed. We strongly encourage further research in this direction, since porosity could be a major difference maker, as it has proven to be for wet-chemical sequential deposition processing. One option to

potentially improve the compactness of the evaporated lead halide layers that we currently contemplate is the evaporation of small amounts PbCl_2 in the future.

3.3. Halide Exchange in Mixed-Halide Layer Stacks

Next, we investigated two mixed-halide sequences. We showed that both Br-1 and Br-split sequences yield a single mixed-halide perovskite $(\text{Cs}, \text{FA})\text{Pb}(\text{I}, \text{Br})_3$ phase.

Both processes exhibited two I-/Br-rich perovskite phases that combined during annealing. Interestingly, the halide exchange reaction between these initial perovskite phases exhibited different speeds for both sequences. When the A cations were between PbBr_2 and PbI_2 in Br-split, Br-rich, and I-rich perovskite phases already formed during evaporation and coexisted significantly longer during annealing compared to Br-1. In Br-1, PbBr_2 and PbI_2 were located adjacent to each other and only an I-rich perovskite phase was observed during evaporation. During annealing, a Br-rich phase formed briefly, but quickly combined with the I-rich phase to form a single perovskite phase. We suspect this to be caused by the low thickness of the initial Br-rich layer, since the perovskite phase is not in direct contact with the PbBr_2 , which provides Br to the perovskite. During annealing of Br-1, PbBr_2 exchanges Br^- ions with I^- ions, enriching the perovskite phase with Br and rendering a segregated PbI_2 phase in the final film.

In Br-split in contrast, the two initial perovskite phases combined comparably slowly. Therefore, it seems that less energy is needed to incorporate Br into an existing I-rich perovskite lattice, than to combine Br- and I-rich perovskite phases. This makes sense, since, in Br-split, both Br^- and the larger I^- ions have to diffuse through the perovskite, whereas this was only Br^- in sequence Br-1. This is supported by previous results, according to which the conversion from MAPbI_3 to MAPbBr_3 is energetically easier than the opposite direction.^[61] Additionally, the diffusion coefficients of Br^- ions in MAPbI_3 were found to be an order of magnitude larger than for I^- ions in MAPbBr_3 ,^[62] adding to the idea that the diffusion of I^- ions slows down the formation of the mixed-halide perovskite in Br-1.

3.4. Absence of δ Phase

In this work in general, we did not once observe a FAPbI_3 δ phase during growth and annealing of our layers using in situ XRD. Feng et al. showed similar results, but do not discuss this effect.^[6] However, the δ phase is the preferred configuration at room temperature and is usually reported to form during co-evaporation, requiring a hot annealing step at 145–170 °C for the conversion into the α phase.^[11,63–65] By employing sequential evaporation and avoiding δ phase formation in the first place, the annealing temperature could be reduced to 100 °C in our work and even 80 °C in others.^[6] This could even be further optimized by creating optimal diffusion reaction conditions through precursor engineering.^[15,44] At first glance, the favored α phase growth could be an intrinsic effect of the diffusion reaction, requiring less energy to transform hexagonal PbI_2 to the cubic perovskite phase than the δ phase, even though the latter is also hexagonal. Nonetheless, we speculate that this behavior is incentivized by

the diffusion limitation of FAI into PbI_2 at room temperature, but not into FAPbI_3 . It follows, that an excess of FAI is present at the interface and during initial perovskite formation, favoring the α phase.^[34–36,65] Still, several open questions in this regard remain, and we hope that this work encourages further investigation in this line.

4. Conclusion

We have prepared $(\text{Cs,FA})\text{PbX}_3$ perovskite layers using a scarcely explored deposition process via sequential thermal evaporation and annealing in a vacuum chamber. This processing route enables ease of scalability and a well-defined stoichiometry control, because the thickness of each individual component can be determined individually. We tested different precursor orders, ratios, and deposition conditions to study their impact on the perovskite conversion dynamics. We observe a barely known PbI_2 6R polytype, and found that this polytype might enhance the conversion. We used in situ XRD to monitor the phase evolution of perovskite components CsI, FAI, PbI_2 , and PbBr_2 during deposition at room temperature and post annealing at 100 °C.

For $(\text{Cs,FA})\text{PbI}_3$, we focused on two sequences: PbI_2 –FAI–CsI (sequence A) and CsI–FAI– PbI_2 (sequence B). In sequence A, PbI_2 grew mainly in its 6R polytype and the stoichiometric layer was fully converted to the perovskite α phase after annealing. However, in the SEM images, we observed voids at the interface to the substrate. Further, when we evaporated different shares of PbI_2 as first and last layers, respectively, we observed void formation at different positions in the stoichiometric layer according to the position of the FAI precursor. In sequence B, PbI_2 growth was dominated by its 2H polytype and void formation did not occur. However, the stoichiometric layer could not be fully converted to the perovskite phase during annealing, unless we deposited an os amount of FAI during the sequence or post deposition.

From the void formation, we deduce that it is FAI that dominantly diffuses into the PbI_2 , while PbI_2 mainly remains at its initial location. CsI will then diffuse into the perovskite lattice. It follows that FAI diffusion and perovskite formation strongly depend on the layer properties and morphology of PbI_2 precursor. Although we cannot pinpoint one decisive property to influence the strong difference in diffusion and reaction behavior in sequences A and B, we assign it to a combination of PbI_2 polytype, (surface) orientation, roughness, and porosity and strongly encourage further research in this direction.

For the deposition of $(\text{Cs,FA})\text{Pb(I,Br)}_3$, we investigated two evaporation sequences: PbBr_2 – PbI_2 –FAI–CsI (Br–1) and PbBr_2 –FAI–CsI– PbI_2 (Br-split). During evaporation, we observed the formation of an I-rich perovskite phase in Br-1, but in total two distinct perovskite phases (I-rich and Br-rich) in Br-split. This resulted in a much faster transition to a single mixed-halide phase in Br-1 compared to Br-split. We relate this to the sterically favored integration of Br^- ions into the I-rich lattice in Br-1, compared to the integration of I^- ions into the Br-rich lattice as in the Br-split experiment.

Astonishingly, we observed no δ phase in all samples throughout sequential evaporation at room temperature and annealing. Therefore, no additional thermal energy is needed to induce the phase transformation from δ to α phase. Consequently,

compared to co-evaporation, a far lower annealing temperature is needed for the perovskite formation, which, in combination with the simplified process control, might provide an important asset in large-scale industrial processing, making sequential evaporation a promising path for further research.

5. Experimental Section

Substrates: We used commercial glass substrates coated with ITO (15 Ωsq , provided by Kintec). Cleaning was done in an ultrasonic bath, subsequently in water with 1% EMAG EM-080 cleaning soap, isopropyl alcohol (IPA), and acetone for 15 min each. For sequences A and B, to produce conditions for perovskite growth on an HTL, a 25 nm thick NiO layer was deposited via e-beam evaporation. Due to an adjustment in process conduct, instead of NiO , Poly(triaryl amine) or Poly[bis(4-phenyl)(2,4,6-trimethylphenyl)amine] (PTAA) was spin-coated from a 5 mg ml^{-1} solution in toluene with 2,3,5,6-tetrafluoro-7,7,8,8-tetracyanoquinodimethane doping for all other samples. After HTL deposition, the samples were transferred to a glove box attached to the in situ evaporation chamber, in which the perovskite layers were evaporated.

Perovskite Deposition: The evaporated materials CsI, PbI_2 (both 99.999%, Thermo Scientific), FAI (>99.5%, Ossila), and PbBr_2 (99.999%, Sigma) were handled in a glove box attached to the evaporation chamber and used as received. We sequentially deposited perovskite layers via thermal evaporation. CsI, FAI, PbI_2 , and PbBr_2 were deposited at 0.5–1, 0.8–1.6, 0.5–1.6, and 0.7–1.2 \AA s^{-1} , respectively. For sequences A, processes with split PbI_2 and B the CsI, FAI, and PbI_2 thicknesses were 21, 224, and 261 nm, resulting in a final nominal composition of $(\text{Cs}_{0.1}\text{FA}_{0.9})\text{PbI}_3$ with a theoretical bandgap energy of 1.5 eV.^[66] When preparing I/Br mixed-halide layers, CsI and FAI thicknesses were kept the same and 115 nm of PbBr_2 and 106 nm of PbI_2 were evaporated yielding the final nominal composition $(\text{Cs}_{0.1}\text{FA}_{0.9})\text{Pb}_{(10.6}\text{Br}_{0.4})_3$ with a theoretical bandgap energy of 1.72 eV.^[66] Thicknesses were monitored using a quartz crystal microbalance. The base pressure of the system was $3 - 4 \cdot 10^{-5}$ mbar owing to the Kapton windows that allow a transmission of X-rays for the in situ XRD measurement. The chamber pressure was monitored with an Edwards WRGS-NW35 wide range gauge and increased to up to 1×10^{-4} mbar during the processes due to thermal radiation of the heated material sources.

XRD Measurement: During evaporation, XRD was measured in situ through exchangeable Kapton windows in the walls of the evaporation chamber. We used $\text{Cu-K}\alpha$ radiation with a wavelength of 1.54 \AA generated at 1.4 kW (35 kV, 40 mA). A linear detector consisting of three Dectris Mythen 1 K modules enabled the measurement of a 28° angular 2 θ range. This was set from 8° to 36° during our experiments. The occurring $\text{K}\beta$ radiation was attenuated by a Ni filter to 5% of the $\text{K}\alpha$ intensity. Using the same setup, we measured θ – θ scans from 10° to 50°. Peak fitting for calculation of the integrated peak area (Int. I) was performed with PDXL version 2.8.1.1 by Rigaku Inc., using a split pseudo-Voigt peak fit.

Film Characterization: SEM was measured using a Zeiss Supra 40 VP. Cross section and top-view images were taken at 1–3 kV employing a secondary electron in-lens detector. In the same SEM, we used a Bruker detector with the EDX analysis program ESPRIT. EDX measurements were done at 10 kV, a working distance of 8 mm, and a magnification of 500. For quantification, Pb M-lines and I, Br, and Cs L-lines were used. A standard-less peak to background (P/B) Z-atomic number, A-absorption correction factor, F-fluorescence correction factor (ZAF) fitting was applied for background correction.

Supporting Information

Supporting Information is available from the Wiley Online Library or from the author.

Acknowledgements

The authors are grateful for the mathematical discussion with Dr. Matthias Maiberg. The German Federal Ministry of Research and Education (BMBF) under contract number 03EK3570B (StrukturSolar II) and the Spanish Ministry of Science and Innovation under contract number (TED2021-129758B-C33) MCIN/AEI/10.13039/501100011033/European Union NextGenerationEU/PRTR provided gratefully acknowledged financial support. P.P. acknowledges funding by the Spanish Ministry of Universities under the Beatriz Galindo Senior program (grant no. BG20/00194). Funding for open access publishing: Universidad Pablo de Olavide/CBUA.

Conflict of Interest

The authors declare no conflict of interest.

Author Contributions

K.H. and T.S. equally contributed to this work. K.H., T.S., and P.P. developed the experimental procedure. P.P. guided the scientific progress. K.H. and T.S. deposited the thin films, and conducted and evaluated the experiments. K.H., T.S., P.P., and R.S. discussed and interpreted the results. K.H. wrote the main part of the manuscript.

Keywords

evaporations, in situ X-ray diffractions (XRDs), perovskites, sequentials

Received: September 8, 2023

Revised: October 31, 2023

Published online: January 16, 2024

- [1] M. A. Green, E. D. Dunlop, M. Yoshita, N. Kopidakis, K. Bothe, G. Siefer, X. Hao, *Prog. Photovolt.: Res. Appl.* **2023**, 31, 651.
- [2] NREL, Best Research-Cell Efficiency Chart, **2023** <https://www.nrel.gov/pv/cell-efficiency.html>.
- [3] J. Wu, X. Xu, Y. Zhao, J. Shi, Y. Xu, Y. Luo, D. Li, H. Wu, Q. Meng, *ACS Appl. Mater. Interfaces* **2017**, 9, 26937.
- [4] Y. Zhang, M. Chen, Y. Zhou, W. Li, Y. Lee, H. Kanda, X.-X. Gao, R. Hu, K. G. Brooks, R. Zia, S. Kinger, N. P. Padture, M. K. Nazeeruddin, *Adv. Energy Mater.* **2020**, 10, 2001300.
- [5] R. Vidal, J.-A. Alberola-Borrás, S. N. Habisreutinger, J.-L. Gimeno-Molina, D. T. Moore, T. H. Schloemer, I. Mora-Seró, J. J. Berry, J. M. Luther, *Nat. Sustain.* **2021**, 4, 277.
- [6] J. Feng, Y. Jiao, H. Wang, X. Zhu, Y. Sun, M. Du, Y. Cao, D. Yang, S. F. Liu, *Energy Environ. Sci.* **2021**, 14, 3035.
- [7] S. Wang, X. Li, J. Wu, W. Wen, Y. Qi, *Curr. Opin. Electrochem.* **2018**, 11, 130.
- [8] J. Ávila, C. Momblona, P. P. Boix, M. Sessolo, H. J. Bolink, *Joule* **2017**, 1, 431.
- [9] J. Li, H. Wang, X. Y. Chin, H. A. Dewi, K. Vergeer, T. W. Goh, J. W. M. Lim, J. H. Lew, K. P. Loh, C. Soci, T. C. Sum, H. J. Bolink, N. Mathews, S. Mhaissalkar, A. Bruno, *Joule* **2020**, 4, 1035.
- [10] K. Hamada, K. Yonezawa, K. Yamamoto, T. Taima, S. Hayase, N. Ooyagi, Y. Yamamoto, K. Ohdaira, *Jpn. J. Appl. Phys.* **2019**, 58, SB SBBF06.
- [11] J. Borchert, R. L. Milot, J. B. Patel, C. L. Davies, A. D. Wright, L. Martínez Maestro, H. J. Snaith, L. M. Herz, M. B. Johnston, *ACS Energy Lett.* **2017**, 2, 2799.
- [12] G. Nogay, F. Sahli, J. Werner, R. Monnard, M. Boccard, M. Despeisse, F.-J. Haug, Q. Jeangros, A. Ingenito, C. Ballif, *ACS Energy Lett.* **2019**, 4, 844.
- [13] M. Kam, Y. Zhu, D. Zhang, L. Gu, J. Chen, Z. Fan, *Sol. RRL* **2019**, 3, 1900050.
- [14] S. Wang, L. Tan, J. Zhou, M. Li, X. Zhao, H. Li, W. Tress, L. Ding, M. Graetzel, C. Yi, *Joule* **2022**, 6, 1344.
- [15] H. Li, J. Zhou, L. Tan, M. Li, C. Jiang, S. Wang, X. Zhao, Y. Liu, Y. Zhang, Y. Ye, W. Tress, C. Yi, *Sci. Adv.* **2022**, 8, 28.
- [16] Z. Zhou, J. Liang, Z. Zhang, Y. Zheng, X. Wu, C. Tian, Y. Huang, J. Wang, Y. Yang, A. Sun, Z. Chen, C.-C. Chen, *ACS Appl. Mater. Interfaces* **2022**, 14, 49886.
- [17] M. F. Mohamad Noh, N. A. Arzaee, I. N. Nawas Mumthas, A. Aadenan, H. Alessa, M. N. Alghamdi, H. Moria, N. A. Mohamed, A. R. B. Mohd Yusoff, M. A. Mat Teridi, *Electrochim. Acta* **2022**, 402, 139530.
- [18] Y. Xiang, Z. Ma, Y. Huang, W. Zhang, C. Peng, H. Li, *ACS Appl. Energy Mater.* **2021**, 4, 12091.
- [19] D. Huang, Q. Liu, Z. Ma, Y. Li, G. Yan, S. Hou, Z. Du, J. Yang, Y. Chen, S. Tang, H. Zhou, Y. Xiang, W. Zhang, Y. Huang, Y. Mai, *Sci. China Mater.* **2023**, 66, 1313.
- [20] Y. Yun Kim, E. Young Park, T.-Y. Yang, J. Hong Noh, T. Joo Shin, N. Joong Jeon, J. Seo, *J. Mater. Chem. A* **2018**, 6, 12447.
- [21] J.-J. Yan, Y. Li, Y. Chang, P. Jiang, C.-W. Wang, *Superlattices Microstruct.* **2016**, 94, 196.
- [22] Y. Wu, A. Islam, X. Yang, C. Qin, J. Liu, K. Zhang, W. Peng, L. Han, *Energy Environ. Sci.* **2014**, 7, 2934.
- [23] J. Burschka, N. Pellet, S.-J. Moon, R. Humphry-Baker, P. Gao, M. K. Nazeeruddin, M. Grätzel, *Nature* **2013**, 499, 316.
- [24] M. T. Hoerantner, E. L. Wassweiler, H. Zhang, A. Panda, M. Nasilowski, A. Osherov, R. Swartwout, A. E. Driscoll, N. S. Moody, M. G. Bawendi, K. F. Jensen, V. Bulović, *ACS Appl. Mater. Interfaces* **2019**, 11, 32928.
- [25] R. S. Mitchell, *Z. für Krist. – Cryst. Mater.* **1959**, 111, 372.
- [26] C. Eames, J. M. Frost, P. R. F. Barnes, B. C. O'Regan, A. Walsh, M. S. Islam, *Nat. Commun.* **2015**, 6, 7497.
- [27] G. Kaune, S. Hartnauer, R. Scheer, *Phys. Status Solidi A* **2014**, 211, 1991.
- [28] N. Nadaud, N. Lequeux, M. Nanot, J. Jové, T. Roisnel, *J. Solid State Chem.* **1998**, 135, 140.
- [29] I. V. Aleksandrov, A. F. Goncharov, I. N. Makarenko, S. M. Stishov, *Phys. Rev. B* **1991**, 43, 6194.
- [30] A. A. Petrov, E. A. Goodilin, A. B. Tarasov, V. A. Lazarenko, P. V. Dorovatovskii, V. N. Khrustalev, *Acta Crystallogr. Sect. E: Crystallogr. Commun.* **2017**, 73, 569.
- [31] D. H. Fabiani, C. C. Stoumpos, G. Laurita, A. Kaltzoglou, A. G. Kontos, P. Falaras, M. G. Kanatzidis, R. Seshadri, *Angew. Chem.* **2016**, 128, 15618.
- [32] C. C. Stoumpos, C. D. Malliakas, M. G. Kanatzidis, *Inorg. Chem.* **2013**, 52, 9019.
- [33] T. Minagawa, *Acta Crystallogr. Sect. A: Cryst. Phys. Diffract. Theoret. Gen. Crystallogr.* **1975**, 31, 823.
- [34] F. Ma, J. Li, W. Li, N. Lin, L. Wang, J. Qiao, *Chem. Sci.* **2017**, 8, 800.
- [35] Z. Yuan, Y. Miao, Z. Hu, W. Xu, C. Kuang, K. Pan, P. Liu, J. Lai, B. Sun, J. Wang, S. Bai, F. Gao, *Nat. Commun.* **2019**, 10, 2818.
- [36] K. L. Heinze, P. Wessel, M. Mauer, R. Scheer, P. Pistor, *Mater. Adv.* **2022**, 3, 8695.
- [37] J. Fang, D. Lin, W. Huang, X. Wang, H. Li, S. Li, G. Xie, D. Wang, L. Qiu, *J. Alloys Compd.* **2023**, 955, 170255.
- [38] Z. Li, J. Li, H. Cao, Y. Qian, J. Zhai, Y. Qiu, L. Yang, S. Yin, *ACS Appl. Mater. Interfaces* **2021**, 13, 45496.
- [39] T. Moser, K. Artuk, Y. Jiang, T. Feurer, E. Gilshtein, A. N. Tiwari, F. Fu, *J. Mater. Chem. A* **2020**, 8, 21973.

- [40] H. E. Swanson, E. Tatge, *Natl. Bur. Stand. U.S.A.* **1953**, 2, 44.
- [41] S. I. Levkovets, O. Y. Khyzhun, G. L. Myronchuk, P. M. Fochuk, M. Piasecki, I. V. Kityk, A. O. Fedorchuk, V. I. Levkovets, L. V. Piskach, O. V. Parasyuk, *J. Electron Spectrosc. Relat. Phenom.* **2017**, 218, 13.
- [42] Q. Guesnay, F. Sahli, C. Ballif, Q. Jeangros, *APL Mater.* **2021**, 9, 100703.
- [43] E. S. Parrott, J. B. Patel, A.-A. Haghighirad, H. J. Snaith, M. B. Johnston, L. M. Herz, *Nanoscale* **2019**, 11, 14276.
- [44] S. Wang, L. K. Ono, M. R. Leyden, Y. Kato, S. R. Raga, M. V. Lee, Y. Qi, *J. Mater. Chem. A* **2015**, 3, 14631.
- [45] D. Yang, Z. Yang, W. Qin, Y. Zhang, S. F. Liu, C. Li, *J. Mater. Chem. A* **2015**, 3, 9401.
- [46] G. Li, J. Y. L. Ho, M. Wong, H.-S. Kwok, *Phys. Status Solidi – Rapid Res. Lett.* **2016**, 10, 153.
- [47] R. Ji, Z. Zhang, C. Cho, Q. An, F. Paulus, M. Kroll, M. Löffler, F. Nehm, B. Rellinghaus, K. Leo, Y. Vaynzof, *J. Mater. Chem. C* **2020**, 8, 7725.
- [48] J. Yan, J. Zhao, H. Wang, M. Kerklaan, L. J. Bannenberg, B. Ibrahim, T. J. Savenije, L. Mazzarella, O. Isabella, *ACS Appl. Energy Mater.* **2023**, 6, 10265.
- [49] I. L. Ivanov, A. S. Steparuk, M. S. Bolyachkina, D. S. Tsvetkov, A. P. Safronov, A. Y. Zuev, *J. Chem. Thermodyn.* **2018**, 116, 253.
- [50] A. Luongo, B. Brunetti, S. Vecchio Cipriotti, A. Ciccio, A. Latini, *J. Phys. Chem. C* **2021**, 125, 21851.
- [51] K. Yonezawa, K. Yamamoto, M. Shahiduzzaman, Y. Furumoto, K. Hamada, T. S. Ripolles, M. Karakawa, T. Kuwabara, K. Takahashi, S. Hayase, T. Taima, *Jpn. J. Appl. Phys.* **2017**, 56, 04CS11.
- [52] M. Shahiduzzaman, K. Yonezawa, K. Yamamoto, T. S. Ripolles, M. Karakawa, T. Kuwabara, K. Takahashi, S. Hayase, T. Taima, *ACS Omega* **2017**, 2, 4464.
- [53] S. Ngqoloda, C. J. Arendse, T. F. Muller, P. F. Miceli, S. Guha, L. Mostert, C. J. Oliphant, *ACS Appl. Energy Mater.* **2020**, 3, 2350.
- [54] Y. Wang, L. Duan, M. Zhang, Z. Hameiri, X. Liu, Y. Bai, X. Hao, *Sol. RRL* **2022**, 6, 2200234.
- [55] B. P. Dhamaniya, P. Chhillar, A. Kumar, K. Chandratre, S. Mahato, K. P. Ganesan, S. K. Pathak, *ACS Omega* **2020**, 5, 31180.
- [56] T. D. Malevu, B. S. Mwankemwa, K. G. Tshabalala, M. Diale, R. O. Ocaya, *J. Mater. Sci.: Mater. Electron.* **2018**, 29, 13011.
- [57] N. Li, Z. Zhu, C.-C. Chueh, H. Liu, B. Peng, A. Petrone, X. Li, L. Wang, A. K.-Y. Jen, *Adv. Energy Mater.* **2017**, 7, 1601307.
- [58] H. A. Abbas, R. Kottokaran, B. Ganapathy, M. Samiee, L. Zhang, A. Kitahara, M. Noack, V. L. Dalal, *APL Mater.* **2015**, 3, 016105.
- [59] A. Liu, K. Liu, H. Zhou, H. Li, X. Qiu, Y. Yang, M. Liu, *Sci. Bull.* **2018**, 63, 1591.
- [60] S. Raza, F. Di Giacomo, F. Matteocci, L. Cinà, A. L. Palma, S. Casaluci, P. Cameron, A. D'Epifanio, S. Licocchia, A. Reale, T. M. Brown, A. Di Carlo, *J. Power Sources* **2015**, 277, 286.
- [61] P. Pistor, T. Burwig, C. Brzuska, B. Weber, W. Fränzel, *J. Mater. Chem. A* **2018**, 6, 11496.
- [62] A. Osherov, Y. Feldman, I. Kaplan-Ashiri, D. Cahen, G. Hodes, *Chem. Mater.* **2020**, 32, 4223.
- [63] Y. Huang, X. Lei, T. He, Y. Jiang, M. Yuan, *Adv. Energy Mater.* **2022**, 12, 2100690.
- [64] M. U. Rothmann, J. S. Kim, J. Borchert, K. B. Lohmann, C. M. O'Leary, A. A. Shearer, L. Clark, H. J. Snaith, M. B. Johnston, P. D. Nellist, L. M. Herz, *Science* **2020**, 370, 6516.
- [65] M. Roß, S. Severin, M. B. Stutz, P. Wagner, H. Köbler, M. Favin-Lévêque, A. Al-Ashouri, P. Korb, P. Tockhorn, A. Abate, B. Stannowski, B. Rech, S. Albrecht, *Adv. Energy Mater.* **2021**, 11, 2101460.
- [66] D. P. McMeekin, G. Sadoughi, W. Rehman, G. E. Eperon, M. Saliba, M. T. Hörlantner, A. Haghighirad, N. Sakai, L. Korte, B. Rech, M. B. Johnston, L. M. Herz, H. J. Snaith, *Science* **2016**, 351, 151.
- [67] F. C. Hanusch, E. Wiesenmayer, E. Mankel, A. Binek, P. Angloher, C. Fraunhofer, N. Giesbrecht, J. M. Feckl, W. Jaegermann, D. Johrendt, T. Bein, P. Docampo, *J. Phys. Chem. Lett.* **2014**, 5, 2791.